

The Origin of Recombining Plasma and the Detection of the Fe-K Line in the Supernova Remnant W28

Hiromichi OKON¹, Hiroyuki UCHIDA¹, Takaaki TANAKA¹, Hideaki MATSUMURA¹ and Takeshi Go TSURU¹

¹Department of Physics, Faculty of Science, Kyoto University, Kitashirakawa Oiwake-cho, Sakyo-ku, Kyoto, Kyoto 606-8502, Japan

*E-mail: okon@cr.scphys.kyoto-u.ac.jp

Received (reception date); Accepted (acceptation date)

Abstract

Overionized recombining plasmas (RPs) have been discovered from a dozen of mixed-morphology (MM) supernova remnants (SNRs). However their formation process is still under debate. As pointed out by many previous studies, spatial variations of plasma temperature and ionization state provide clues to understand the physical origin of RPs. We report on a spatially resolved X-ray spectroscopy of W28, which is one of the largest MM SNRs found in our Galaxy. Two observations with Suzaku XIS cover the center of W28 to the northeastern rim where the shock is interacting with molecular clouds. The X-ray spectra in the inner regions are well reproduced by a combination of two-RP model with different temperatures and ionization states, whereas that in northeastern rim is explained with a single-RP model. Our discovery of the RP in the northeastern rim suggests an effect of thermal conduction between the cloud and hot plasma, which may be the production process of the RP. The X-ray spectrum of the northeastern rim also shows an excess emission of the Fe I $K\alpha$ line. The most probable process to explain the line would be inner shell ionization of Fe in the molecular cloud by cosmic-ray particles accelerated in W28.

Key words: ISM: individual objects (W28, G6.4–0.1) — ISM: supernova remnants — cosmic rays — X-rays: ISM

1 Introduction

W28 (a.k.a., G6.4–0.1) is one of the most well-studied Galactic supernova remnants (SNRs) interacting with molecular clouds (Wootten 1981). The remnant is also known as one of the typical mixed-morphology (MM) SNRs which are characterized by a radio shell with center-filled X-rays (Rho & Petre 1998). Due to its old age (33–42 kyr; Kaspi et al. 1993; Velázquez et al. 2002; Li & Chen 2010) and a relatively small distance (~ 2 kpc based on the H I observation; Velázquez et al. 2002), W28 has a large apparent size of $\sim 48'$ (Seward 1990), which enables us to investigate the small physical scale structures associated with this SNR.

W28 appears to be expanding into a dense interstellar medium (ISM) as suggested by a global structure of H I gas (Velázquez et al. 2002). Nobukawa et al. (2018) found the Fe I $K\alpha$ emission roughly coincident with the H I distribution, indicating possible interactions between low-energy cosmic-ray protons (LECRp) and the dense ISM in the vicinity of W28. Also, as first suggested by Wootten (1981), many previous studies provided evidence that the northeastern part of W28 is interacting with a dense molecular cloud. These studies include detections of OH maser (1720 MHz) spots (Frail et al. 1994; Claussen et al. 1997), the presence of shocked gas traced by ^{12}CO ($J = 3 - 2$) and ^{12}CO ($J = 1 - 0$) lines (Arikawa et

al. 1999), and GeV/TeV gamma-ray emission coincident with these molecular clouds (Aharonian et al. 2008; Abdo et al. 2010; Giuliani et al. 2010).

Past observations of W28 with ROSAT and ASCA revealed a centrally concentrated X-ray emission as well as a bright northeastern X-ray rim (Rho & Borkowski 2002). Recently, Sawada & Koyama (2012) observed the central region of W28 with Suzaku and discovered an overionized recombining plasma (RP), which was supported by a Chandra observation of the same region (Pannuti et al. 2017). While the formation process of the RP is poorly understood, one of the possible scenarios is a thermal conduction between SNRs and surrounding molecular clouds (Kawasaki et al. 2002). Although Sawada & Koyama (2012) prefer another possible scenario “rarefaction” (Itoh & Masai 1989; Shimizu et al. 2012), a more comprehensive spatially resolved study is required to approach the true origin of the RP in W28.

The gas environment in the vicinity of SNRs is a key to understanding the physical origin of the RPs for both scenarios (Itoh & Masai 1989; Kawasaki et al. 2002). Supportive evidence for the thermal conduction scenario is found from two RP SNRs, G166.0+4.3 (Matsumura et al. 2017a) and IC 443 (Matsumura et al. 2017b). Their main argument is that X-ray emitting plasmas surrounded by dense ISM or molecular clouds are significantly cooled and are in the recombining state. In this context, the bright northeastern rim of W28 is also expected to be overionized. Nakamura et al. (2014) and Zhou et al. (2014), however, reported no detection of an RP from the X-ray spectrum of the northeastern rim obtained with XMM-Newton, which may conflict with the thermal conduction scenario. Since the RP has been robustly detected from the central region by Sawada & Koyama (2012), it is required to investigate the spatial variation of temperature and ionization state from the center toward the northeastern rim.

In this paper, we report on the result of a spatially resolved analysis of the central to the northeastern parts of W28 with Suzaku. The Suzaku observation of the northeastern part is analyzed in our paper for the first time. Strong K-shell emissions from neutral and highly ionized Fe are detected from the northeastern bright rim and the center of W28, respectively. Both are key to understanding the formation process of RPs and the interaction between the northeastern rim and surrounding molecular clouds. Throughout the paper, errors are quoted at 90% confidence levels in the tables and text. Error bars shown in the figures are 1σ confidence levels. The distance to W28 is assumed to be 2 kpc (Velázquez et al. 2002).

2 Observations and data reduction

Two-pointing observations (the center and the northeast) of W28 were carried out with Suzaku in 2010 April and 2011

February, respectively. The observation log is summarized in table 1. We analyzed data taken with the X-ray Imaging Spectrometer (XIS; Koyama et al. 2007) aboard Suzaku. The XIS is composed of four CCD cameras (XIS0, 1, 2, and 3), which are installed on the focal planes of the X-Ray Telescopes (XRTs; Serlemitsos et al. 2007). XIS2 and a segment of XIS0 have malfunctioned and been out of operation since 2006 November and 2009 June, respectively (Suzaku XIS documents^{1,2}).

We reduced the data with the HEADAS software version 6.19 and the calibration database released in 2016 June. We selected events with the standard event selection criteria provided by the Suzaku team. We estimated the non-X-ray background (NXB) with `xisnxbgen` (Tawa et al. 2008). We generated the redistribution matrix files and the ancillary response files by using `xismfgen` and `xissimarfgen` (Ishisaki et al. 2007), respectively. We used version 12.9.0u of the XSPEC software (Arnaud 1996) for the following spectral analysis. For analyzing the XIS0 and XIS3 data, we ignored the energy band of 1.7–2.0 keV because of the calibration uncertainty around the neutral Si K-edge (Suzaku XIS documents³).

3 Analysis and results

3.1 Image

Figure 1 shows an NXB-subtracted and vignetting and exposure corrected image of W28 (0.65–4.0 keV). The centrally peaked morphology is seen at the SNR’s center, where Sawada & Koyama (2012) found the RP. The rim-brightened partial shell (Rho & Borkowski 2002) is present in the northeastern region, where Nakamura et al. (2014) and Zhou et al. (2014) found no evidence for an RP. The interior region between the center and the northeastern rim can further be divided into two parts: the northern part where a shock-cloud interaction is suggested from the ^{12}CO and OH maser emissions and the southern part where molecular clouds were not found through past observations. In order to investigate the spatial association between plasma parameters and the ambient molecular clouds, we thus selected four regions which are enclosed by the cyan lines in figure 1.

3.2 Fe lines

W28 is located near the Galactic center, where the Galactic ridge X-ray emission (GRXE) is not negligible especially in the high energy band. Figure 2 shows NXB-subtracted XIS spectra taken from the four regions. We detected emission lines of Fe $K\alpha$ in the 6.0–7.0 keV band as well as the Ne, Mg, Si and S K

¹ <ftp://legacy.gsfc.nasa.gov/suzaku/doc/xis/suzakumemo-2007-08.pdf>

² <ftp://legacy.gsfc.nasa.gov/suzaku/doc/xis/suzakumemo-2010-01.pdf>

³ <https://heasarc.gsfc.nasa.gov/docs/suzaku/analysis/sical.html>

Table 1. Observation log.

Target	Obs. ID	Obs. date	(R.A., Dec.)*	Effective exposure (ks)
W28_CENTER	505005010	2010-Apr-03	(18 ^h 00 ^m 17 ^s , −23°21′59″)	73.0
W28_NE	505006010	2011-Feb-25	(18 ^h 01 ^m 30 ^s , −23°17′30″)	100

* Equinox in J2000.0.

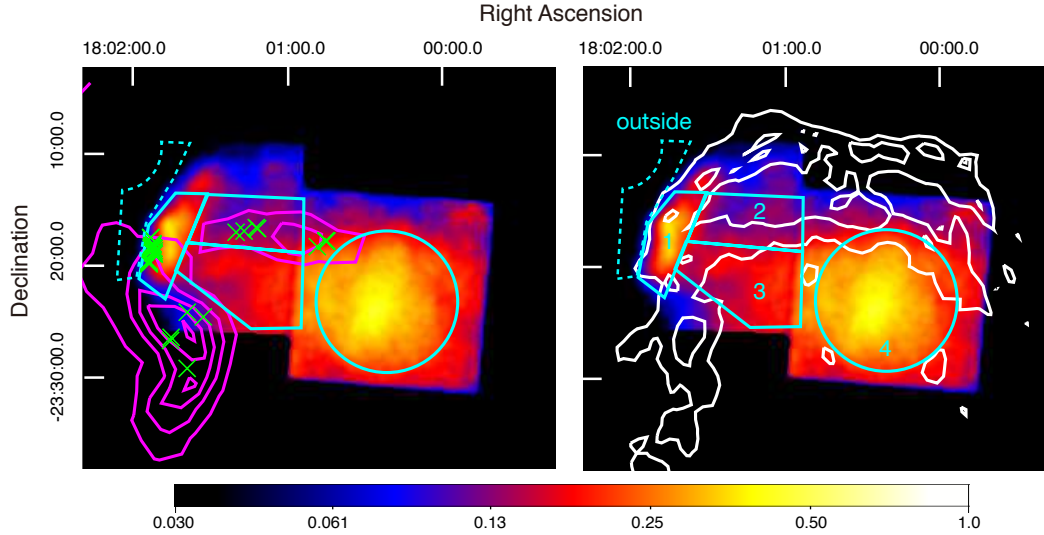


Fig. 1. Images of W28 in the energy band of 0.65–4.0 keV after NXB subtraction and vignetting effect and exposure correction. The cyan solid and dash lines denote the source and background regions, respectively. In the left panel, the magenta contours indicate the distribution of the ^{12}CO ($J = 2 - 1$) line emissions for $V_{\text{LSR}} = -15 \text{ km s}^{-1}$ to 15 km s^{-1} as observed with the NANTEN2 telescope (Torii et al. 2011). The magenta contours are drawn every 40 K km s $^{-1}$ from 40 K km s $^{-1}$. The 1720 MHz OH maser emission (Claussen et al. 1997) detected at the locations indicated by the green crosses are taken with the Karl G. Jansky Very Large Array (VLA). In the right panel, the radio 325 MHz image shown as the white contours are taken with VLA. The white contours are drawn every 0.225 Jy/beam from 0.05 Jy/beam.

α lines in the low energy band. As shown in the lower panel of figure 2, there are two prominent lines around $\sim 6.5 \text{ keV}$. The measured line centroids are $6370^{+30}_{-15} \text{ eV}$ and $6671^{+11}_{-10} \text{ eV}$, which are consistent with those of Fe I $K\alpha$ (6.40 keV) and Fe XXV $\text{He}\alpha$ (6.68 keV), respectively. It is reasonable to consider that they are *mostly* attributed to the GRXE since the SNR emission (Sawada & Koyama 2012) and a possible non-thermal emission including the Fe I $K\alpha$ line produced by LECRp (Nobukawa et al. 2018) are both relatively weak as noted by these studies. We, however, carefully evaluated the contributions of each component as described below.

Figure 3 presents the Fe I $K\alpha$ and Fe XXV $\text{He}\alpha$ intensities of each region measured by fitting the 6.0–7.5 keV spectra with a phenomenological model: a power-law continuum plus four Gaussians at 6.40 keV (Fe I $K\alpha$), 6.68 keV (Fe XXV $\text{He}\alpha$), 6.97 keV (Fe XXVI $\text{Ly}\alpha$), and 7.06 keV (Fe I $K\beta$). We plot, for comparison, the intensities of a region outside W28 (“outside”; see figure 1). We found that the intensities of both lines are almost consistent with the GRXE level in the outside region, whereas the Fe I $K\alpha$ and Fe XXV $\text{He}\alpha$ lines are relatively strong in region 1 and region 4, respectively. As pointed out by Rho & Borkowski (2002), hard emission is concentrated on the center of the remnant. We thus expect the presence of a high temper-

ature plasma in region 4, which is able to emit the Fe XXV $\text{He}\alpha$ line. On the other hand, the Fe I $K\alpha$ excess is significant only in region 1 where the shock is interacting with the clouds. The result implies a similar Fe I $K\alpha$ enhancement reported for several Galactic SNRs (Sato et al. 2014; Sato et al. 2016; Nobukawa et al. 2018). This point will be discussed in more detail in section 4.2.

3.3 Local X-ray Background

We first estimated the background spectrum from a nearby blank-sky data (Obs ID: 500008010) following Sawada & Koyama (2012). However, the background level of the blank-sky data above 4 keV is significantly higher than the total flux of the W28 regions in the same energy band, although it is within the global fluctuation of the GRXE presented by Uchiyama et al. (2013). Note that Sawada & Koyama (2012) only used the data below 5 keV for their spectral analysis. We speculate that, in this case, the discrepancy of the GRXE levels between the two observations could be negligible. On the other hand, we found significant contributions from the thermal emission from W28 around the Fe XXV $\text{He}\alpha$ line as explained above. We therefore used another local background extracted from a source-free

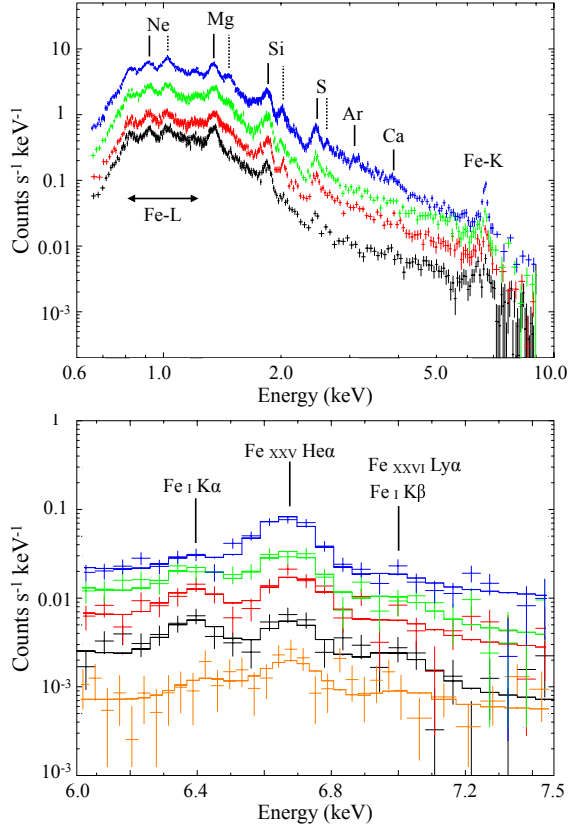


Fig. 2. Spectra of regions outside (orange), 1 (black), 2 (red), 3 (green), and 4 (blue) in the energy band of 0.65–4.0 keV (upper) and 6.0–7.5 keV (lower) obtained with the XIS0 + 3. NXB was subtracted. The spectra of regions outside, 2, 3, and 4 are scaled by factors of 0.5, 2.0, 3.0, and 2.0, respectively, for display purpose. The vertical solid and dashed black lines in the top panel represent the centroid energies of the He α lines, Ly α lines, respectively. The vertical solid lines in the bottom panel denote the centroid energies of the Fe-K lines.

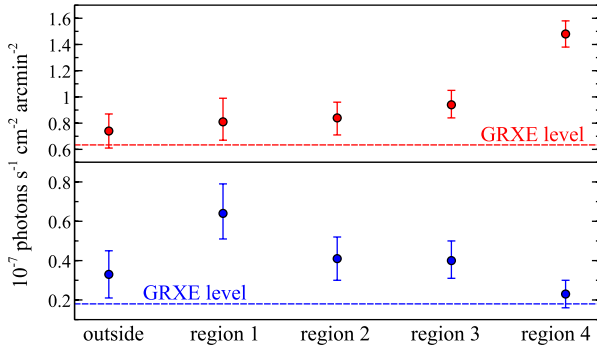


Fig. 3. Intensities of Fe-K α lines of the five regions obtained by fitting the spectra of the five regions with the phenomenological model. The red and blue points represent the intensities of Fe XXV He α line and the Fe I K α line, respectively. The horizontal dashed lines indicate the GRXE level (Yamauchi et al. 2016).

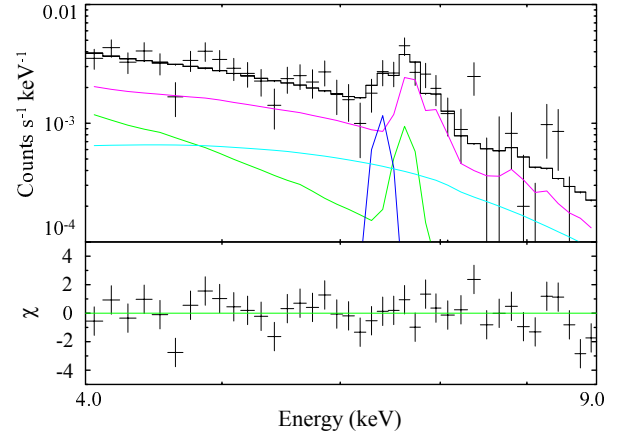


Fig. 4. Spectrum of outside region in the energy band of 4.0–9.0 keV obtained with the XIS0 + 3. The black lines represent the best-fit model, which are decomposed into each component indicated with the colored curves. The magenta, green, cyan and blue lines represent the HP, LP, CXB and Fe I K α line components, respectively.

region of our observations, namely “outside” shown in figure 1, in the following analysis.

Figure 4 shows the 4.0–9.0 keV spectrum obtained from the outside region. We applied a background model consisting of the GRXE and the cosmic X-ray background (CXB). The parameters for the CXB component were fixed to the values given by Kushino et al. (2002). Considering the results by Uchiyama et al. (2013) and Yamauchi et al. (2016), we made a semi-phenomenological GRXE model composed of the foreground emission (FE), the high-temperature plasma (HP) and the low-temperature plasma (LP) from the Galactic ridge and the Fe I K α line from the Galactic plane. We fixed the parameters of the LP and HP to the values of Uchiyama et al. (2013), except for kT_e of the HP and normalization of the HP and LP. The normalization of the HP was fixed at 0.29 times that of the LP (Uchiyama et al. 2013). The electron temperature kT_e and normalization of the LP were free parameters. The intensity of the Fe I K α line was also allowed to vary, whereas that of the Fe I K β to K α intensity ratio was fixed to 0.125 (Kaastra & Mewe 1993). The best-fit model is shown in figure 4 and the best-fit parameters are summarized in table 2. We used this model as the background spectrum for W28.

3.4 Spectral Analysis

Following the results by Zhou et al. (2014) and Nakamura et al. (2014) on the northeastern rim, we first tried an absorbed non-equilibrium ionization (NEI) model for the spectra of region 1. We applied the Wisconsin absorption model (Morrison & McCammon 1983) with solar abundances (Anders & Grevesse 1989) with the column density N_H allowed to vary. The electron temperature kT_e , ionization time scale $n_e t$ and

Table 2. Best-fit model parameters of the background.

Component	Parameter (unit)	Value
FE _{low}	kT_e (keV)	0.09 (fixed)
	Z_{all} (solar)	0.05 (fixed)
	VEM (10^{59} cm^{-3}) [†]	1.8 (fixed)
FE _{high}	kT_e (keV)	0.59 (fixed)
	Z_{all} (solar)	0.05 (fixed)
	VEM (10^{56} cm^{-3}) [†]	6.7 (fixed)
CXB	N_{H} (10^{22} cm^{-2})	8.44 (fixed)
	Photon index	1.4 (fixed)
	Normalization [‡]	9.69 (fixed)
LP	kT_e (keV)	1.33 (fixed)
	Z_{Ar} (solar)	1.07 (fixed)
	Z_{other} (solar)	0.81 (fixed)
	VEM (10^{56} cm^{-3}) [†]	6.5 ± 0.7
HP	kT_e (keV)	$7.5^{+2.7}_{-1.7}$
	Z_{Ar} (solar)	1.07 (fixed)
	Z_{other} (solar)	0.81 (fixed)
	VEM (10^{56} cm^{-3}) [†]	$0.29 \times \text{LP VEM}$ (fixed)
$\chi^2_\nu (\nu)$ [§]		1.42 (76)

[†] Volume emission measure $\text{VEM} = \int n_e n_{\text{H}} dV$, where n_e , n_{H} , and V are the electron density, the hydrogen density, and the emitting volume, respectively.

[‡] The unit is photons $\text{s}^{-1} \text{ cm}^{-2} \text{ keV}^{-1} \text{ sr}^{-1}$ at 1 keV.

[§] The parameters χ^2_ν and ν indicate a reduced chi square and a degree of freedom, respectively.

normalization of the NEI component were allowed to vary. The abundances of Ne, Mg, Si, S and Fe were also set free, whereas Ar and Ca were linked to S, and Ni was linked to Fe. The abundances of all the other elements were fixed to solar. As explained in section 3.3, the parameters of the background model were fixed to the values presented in table 2, while the normalization of the Fe I-K lines was allowed to vary. Note that the best-fit values of the Fe I-K lines are consistent with those displayed in figure 3 and in table 3. Figure 5 (1-i) shows the result. The result yields a large $n_e t \geq 3 \times 10^{12} \text{ cm}^{-3} \text{ s}$, which prefers a collisional ionization equilibrium (CIE; Masai 1994). However, this model is statistically unacceptable ($\chi^2_\nu = 2.16$ with $\nu = 341$). We found that large residuals are still seen below 2 keV, especially at ~ 1.5 keV around the Mg XII Ly α line, indicating that a higher ionization state is required for the plasma in region 1.

We therefore applied an RP model, where an initial temperature kT_{init} was allowed to vary in addition to the above free parameters. We linked S to Si since these abundances are consistent within the 90% error margin. As shown in figure 5 (1-ii), the RP model considerably improved the residuals below 2 keV other than an excess 1.2 keV line ($\chi^2_\nu = 1.44$ with $\nu = 339$). We consider that the excess is due to the lack of Fe-L lines in a current plasma code, as pointed out by a number of previous studies (e.g., Hughes et al. 1998, Borkowski et al. 2006, Yamaguchi et al. 2011). Adding a Gaussian at 1.23 keV, we refitted the spectrum and obtained a statistically good fit as shown

in figure 5 (1-iii) ($\chi^2_\nu = 1.31$ with $\nu = 338$). The best-fit parameters are listed in table 4. Note that our result is inconsistent with the results of XMM-Newton (Zhou et al. 2014; Nakamura et al. 2014). This is simply because the excess of the Mg XII Ly α emission we found is relatively weak, which cannot be correctly measured in the statistically poorer (< 30 ks) EPIC spectra they analyzed.

We next analyzed the spectrum of region 4. Following the result given by Sawada & Koyama (2012), we also fitted the spectrum with a similar RP model as explained above. With the RP model, we cannot reproduce the spectrum ($\chi^2_\nu = 5.15$ with $\nu = 346$). In figure 5 (4-i), large residuals appear below 3 keV, particularly at ~ 0.9 keV and ~ 1.0 keV, corresponding to the Ne IX He α and the Ne X Ly α lines, respectively. On the other hand, the model gives a fairly good fit above 3 keV. These results naturally indicate that required ion populations (i.e., ionization states) are different between the soft-band and hard-band spectra. We therefore tried a two-RP model with different ionization states; neither an NEI+RP model nor a CIE+RP model can reproduce the spectrum particularly below 1 keV ($\chi^2_\nu = 2.03$ with $\nu = 336$ and $\chi^2_\nu = 2.04$ with $\nu = 338$, respectively). We linked the abundances and kT_{init} of the two components because these parameters are within 90% error margin when we thawed them. As shown in figure 5 (4-ii) and summarized in table 4, the two-RP model explained well the spectrum of region 4 ($\chi^2_\nu = 1.71$ with $\nu = 343$).

Since regions 2 and 3 are located between region 1 and region 4, we expect that their spectra should be described by a similar model with those for regions 1 or 4. We thus tried two different models: single RP and two-RP. The single-RP model results in large residuals in the soft energy band (< 1 keV) whereas the two-RP model gives a statistically acceptable fit, as displayed in figures 5 (2) and (3). The detailed parameters are summarized in table 4.

4 Discussion

As best fit in the previous section, the X-ray spectra are explained by a single RP (region 1: the northeastern rim) or two-component RP (regions 2, 3 and 4: the inside) models. Based on the best-fit results, we plot the absorption column density N_{H} , electron temperature kT_e , and ionization timescale $n_e t$ of the RP components in figure 6.

4.1 Gas Environment of W28

As indicated in figure 6, the absorption column density N_{H} is significantly higher in regions 1 and 2 than those in regions 3 and 4. The values are consistent with the previous X-ray studies for each region (Pannuti et al. 2017; Nakamura et al. 2014; Zhou et al. 2014). The spatial variation of N_{H}

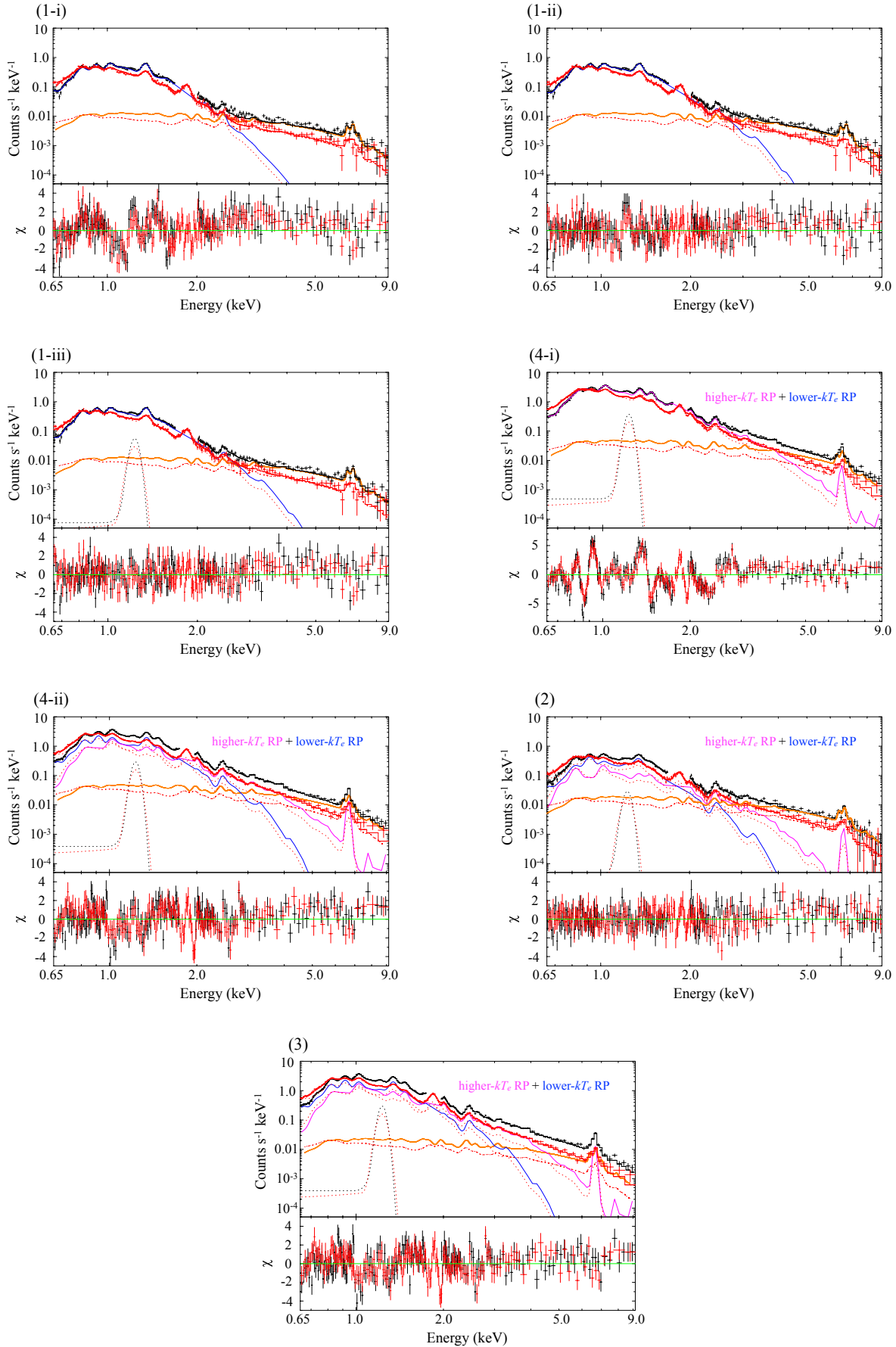


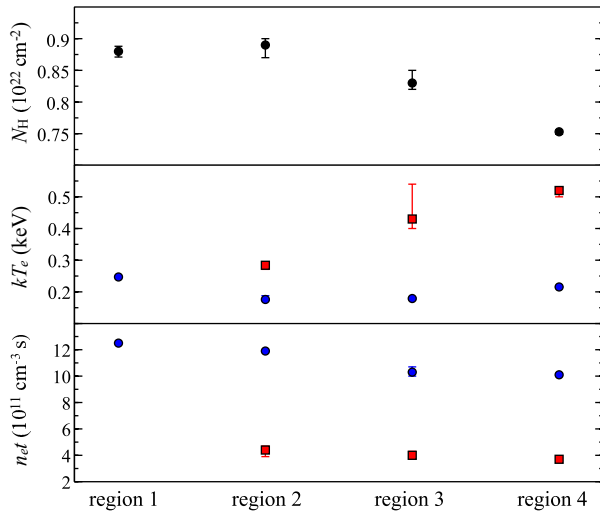
Fig. 5. Spectra of regions 1, 2, 3, and 4 in the energy band of 0.65–4.0 keV. The black and red data points show the XIS0+3 (FI) and XIS1 (BI) spectra, respectively. The magenta, blue and orange curves represent the higher- kT_e RP, the lower- kT_e RP and the background for the FI spectra, respectively. The dotted curves are the Gaussian for the Fe-L lines at 1.23 keV.

Table 3. The 4.0–9.0 keV surface brightness and intensities and of Fe lines[†].

line	outside	region 1	region 2	region 3	region 4
Fe I K α	$0.33^{+0.19}_{-0.20}$	$0.64^{+0.24}_{-0.22}$	$0.41^{+0.18}_{-0.17}$	0.40 ± 0.16	$0.23^{+0.11}_{-0.09}$
Fe XXV He α	0.74 ± 0.22	$0.81^{+0.29}_{-0.24}$	$0.84^{+0.19}_{-0.20}$	0.94 ± 0.18	1.48 ± 0.15

[†]The units is 10^{-7} photons s^{-1} cm^{-2} arcmin $^{-2}$.**Table 4.** Best-fit model parameters of SNR plasmas.

Model function	Parameter (unit)	(region 1)	(region 2)	(region 3)	(region 4)
Absorption	N_H (10^{22} cm $^{-2}$)	$0.88^{+0.02}_{-0.03}$	$0.89^{+0.03}_{-0.02}$	$0.83^{+0.03}_{-0.02}$	0.75 ± 0.01
VVRNEI1	kT_e (keV)	$0.247^{+0.05}_{-0.07}$	0.18 ± 0.01	$0.179^{+0.011}_{-0.004}$	$0.216^{+0.001}_{-0.005}$
	kT_{init} (keV)	≥ 2.4	$3.7^{+1.1}_{-0.9}$	$3.5^{+1.0}_{-0.8}$	$3.8^{+0.4}_{-0.6}$
	Z_{Ne} (solar)	1.3 ± 0.1	$1.7^{+0.2}_{-0.3}$	$2.0^{+0.2}_{-0.1}$	$1.73^{+0.07}_{-0.06}$
	Z_{Mg} (solar)	$1.14^{+0.09}_{-0.08}$	1.3 ± 0.2	1.5 ± 0.1	$1.57^{+0.05}_{-0.04}$
	Z_{Si} (solar)	1.1 ± 0.1	1.3 ± 0.2	1.3 ± 0.2	1.4 ± 0.1
	$Z_S = Z_{Ar} = Z_{Ca}$ (solar)	$= Z_{Si}$	$1.7^{+0.3}_{-0.2}$	1.6 ± 0.3	1.38 ± 0.07
	$Z_{Fe} = Z_{Ni}$ (solar)	1.0 ± 0.1	2.4 ± 0.7	2.9 ± 0.3	$1.17^{+0.03}_{-0.05}$
	$n_e t$ (10^{11} cm $^{-3}$ s)	$12.5^{+0.01}_{-0.02}$	$11.8^{+1.2}_{-0.7}$	$10.2^{+0.8}_{-0.4}$	10.1 ± 0.2
	VEM (10^{57} cm $^{-3}$) [†]	$5.3^{+0.4}_{-0.6}$	8^{+1}_{-2}	$11^{+0.3}_{-0.1}$	16^{+1}_{-1}
VVRNEI2	kT_e (keV)	-	$0.28^{+0.03}_{-0.02}$	$0.43^{+0.21}_{-0.07}$	$0.52^{+0.01}_{-0.02}$
	$n_e t$ (10^{11} cm $^{-3}$ s)	-	4.4 ± 0.8	$4.0^{+0.5}_{-0.6}$	$3.7^{+0.2}_{-0.1}$
	VEM (10^{57} cm $^{-3}$) [†]	-	$0.7^{+0.3}_{-0.2}$	$0.4^{+0.1}_{-0.2}$	2.2 ± 0.2
Gaussian	Centroid (keV)	1.23 (fixed)	1.23 (fixed)	1.23 (fixed)	1.23 (fixed)
	Normalization [‡]	1.6 ± 0.3	0.6 ± 0.3	0.7 ± 0.2	1.6 ± 0.2
χ^2_ν (ν)		1.31 (338)	1.15 (347)	1.58 (343)	1.71 (343)

[†] Volume emission measure VEM = $\int n_e n_H dV$, where n_e , n_H , and V are the electron density, the hydrogen density, and the emitting volume, respectively.[‡] The unit is 10^{-6} photons s^{-1} cm^{-5} arcmin $^{-2}$.**Fig. 6.** N_H (upper), kT_e (middle) and $n_e t$ (lower) of the two RP components obtained for the four regions. The red and blue points represent the parameters for the higher- kT_e RPs and those for the lower- kT_e RPs, respectively.

roughly correlates with the ^{12}CO ($J = 2 - 1$) emission and the 1720 MHz OH maser spots (figure 1). A position-velocity diagram of CO ($J = 3 - 2$) given by Arikawa et al. (1999) suggests that the molecular cloud is associated with W28 and is situated in front of the remnant. According to Aharonian et al. (2008), the ^{12}CO ($J = 1 - 0$) observation with NANTEN2 in-

dicates that a part of the cloud is in front of the remnant in the northeastern region. Our X-ray analysis confirms their results: the northeastern part (regions 1 and 2) of W28 is largely obscured by the molecular cloud interacting with the remnant.

4.2 Origin of Neutral Fe-K Line

As shown in figure 3, we detected a line excess at 6370^{+30}_{-15} eV in region 1, where W28 is interacting with the molecular cloud. Although one possible origin of this line is thermal emission from the remnant, it is less plausible because W28 is one of the middle-aged and core-collapse SNRs, from which K α lines of nearly-neutral Fe are generally not expected (Yamaguchi et al. 2014). An alternative possibility is that accelerated cosmic-ray particles bombard the northeastern cloud and emit the enhanced Fe I K α line emissions. A similar interpretation was proposed by Sato et al. (2014) and Sato et al. (2016) in the cases of two other mixed-morphology SNRs, 3C 391 and Kes 79, respectively. Since GeV/TeV γ -ray observations of W28 provide evidence for the presence of particle acceleration (Abdo et al. 2010; Aharonian et al. 2008), this scenario would be more likely. Further evidence is provided by Nobukawa et al. (2018), who reported that enhanced Fe I K α line emissions are detected from four Galactic SNRs (Kes 67, Kes 69, Kes 78 and W44) and also from the central region of W28.

4.3 Recombining Plasma

As presented in section 3.4, our results clearly suggest that two RP plasmas with different temperatures are required for the inner regions (2, 3, and 4). From figure 6, the “cold” component has an electron temperature $kT_e \sim 0.2$ keV whereas the “hot” component has a much higher temperature 0.3–0.5 keV. The temperature of the hot component in region 2 is close to that of the cold component and is the lowest among the three inner regions. On the other hand, the spectrum of region 1 is adequately represented by a single RP component with $kT_e \sim 0.25$ keV. It is notable that the temperature in region 1 is close to the average temperature in region 2. Taking account of the gas environment discussed in the previous section, we presume that these results hint at the physical structure of the plasma in W28: the temperature in the northeast has decreased due to the dense surrounding environment which gradually cools the remnant toward the center.

A similar picture was proposed by Matsumura et al. (2017b), who indicated that IC 443 is cooled in the southeastern region where the blast waves are in contact with molecular clouds. We point out that both W28 and IC 443 are the MM SNRs largely dominated by RPs. Since all the RP SNRs discovered so far are classified as MM SNRs (see table 4 in Uchida et al. 2015) that show strong evidence for SNR-cloud interaction (Rho & Petre 1998), it is reasonable to assume thermal conduction as a possible scenario to create the RP. As discussed by Kawasaki et al. (2002), the RP can arise from thermal conduction between the hot ejecta and dense surrounding environment when the cooling timescale is shorter than the recombination timescale. While Sato et al. (2014) and Washino et al. (2016) focused on thermal conduction between the downstream shocked material and the upstream neutral gas, it is generally difficult to calculate an accurate timescale since a saturated conduction may not be negligible near the contact surface of the shock front (Dalton & Balbus 1993). On the other hand, White & Long (1991) proposed a cloud evaporation model to account for the center-filled morphology of MM SNRs. Zhou et al. (2011) also presumed that the northeastern rim is a product of cloud evaporation. If this is the case, the evaporation scenario may be a potential origin of the overionization. However, current simulations are too simple to predict the spectrum expected in this scenario; to discuss the true origin of RPs, the inclusion of more physical processes (e.g., non-equilibrium ionization) is required in future works (Slavin et al. 2017).

Sawada & Koyama (2012) favored another plausible origin of the RP, namely rarefaction (Itoh & Masai 1989; Shimizu et al. 2012). According to several calculations (Itoh & Masai 1989; Shimizu et al. 2012), the blast wave should have broken out of the circumstellar material less than several 100 yr after the explosion (Moriya 2012). The timescale is much shorter than the estimated age of W28, 33–42 kyr (Velázquez

et al. 2002; Kaspi et al. 1993; Li & Chen 2010). From the best-fit value of $n_e t$ presented in table 4, we estimated the elapsed time since the rarefaction to be $11 \times (n_e / 1 \text{ cm}^{-3})^{-1}$ kyr and $32 \times (n_e / 1 \text{ cm}^{-3})^{-1}$ kyr for the high- kT_e RP and the low- kT_e RP in region 4, respectively. We note that the result is roughly consistent with the estimation given by Sawada & Koyama (2012), $\sim 10 \times (n_e / 1 \text{ cm}^{-3})^{-1}$ kyr. These timescales are on the same order of the age of W28, indicating that the rarefaction scenario cannot be ruled out. In this scenario, however, the spatial variations of temperature and ionization state are difficult to explain, as previously noted by Sawada & Koyama (2012).

5 Conclusion

We analyzed the Suzaku XIS data of the central and north-eastern regions of W28. In the spatially resolved analysis, we found that each spectrum is best explained by an RP model. The X-ray spectra in the inner regions are well reproduced by a combination of two RPs; a cold low-ionized ($kT_e \sim 0.2$ keV, $n_e t \sim 10^{12} \text{ cm}^{-3} \text{ s}$) and a hot highly ionized ($kT_e \geq 0.3$ keV, $n_e t \sim 4 \times 10^{11} \text{ cm}^{-3} \text{ s}$) components. On the other hand, the spectrum of the northeastern rim is represented by a single RP with $kT_e \sim 0.25$ keV. The spatial variations of these parameters suggest that a thermal conduction (e.g., cloud evaporation scenario) is the origin of the overionization, although we cannot rule out the rarefaction scenario as an alternative scenario. We also found the Fe I K α line only in the northeastern rim region, suggesting possible interactions between cosmic-ray particles and the molecular cloud.

Acknowledgments

We are grateful to Dr. Makoto Sawada for helpful advice. We thank Dr. Satoshi Yoshiike for providing us with the NANTEN2 data. We deeply appreciate all the Suzaku team members. This work is supported by JSPS/MEXT Scientific Research Grant Numbers JP15J01842 (H.M.), JP25109004 (T.T. and T.G.T.), JP26800102 (H.U.), JP15H02090 (T.G.T.), and JP26610047 (T.G.T.).

References

- Abdo, A. A., Ackermann, et al. 2010, *ApJ*, 718, 348
- Aharonian, F., et al. 2008, *A&A*, 481, 401
- Anders, E., & Grevesse, N. 1989, *Geochim. Cosmochim. Acta*, 53, 197
- Arnaud, K. A. 1996, *Astronomical Data Analysis Software and Systems V*, 101, 17
- Arikawa, Y., Tatematsu, K., Sekimoto, Y., & Takahashi, T. 1999, *PASJ*, 51, L7
- Borkowski, K. J., Hendrick, S. P., & Reynolds, S. P. 2006, *ApJ*, 652, 1259
- Claussen, M. J., Frail, D. A., Goss, W. M., & Gaume, R. A. 1997, *ApJ*, 489, 143
- Dalton, W. W., & Balbus, S. A. 1993, *ApJ*, 404, 625
- Frail, D. A., Goss, W. M., & Slysh, V. I. 1994, *ApJ*, 424, L111
- Giuliani, A., et al. 2010, *A&A*, 516, L11

- Hughes, J. P., Hayashi, I., & Koyama, K. 1998, *ApJ*, 505, 732
- Itoh, H., & Masai, K. 1989, *MNRAS*, 236, 885
- Ishisaki, Y., et al. 2007, *PASJ*, 59, 113
- Kaastra, J. S., & Mewe, R. 1993, *A&AS*, 97, 443
- Kaspi, V. M., Lyne, A. G., Manchester, R. N., Johnston, S., D'amico, N., & Shemar, S. L. 1993, *ApJ*, 409, L57
- Kawasaki, M. T., Ozaki, M., Nagase, F., Masai, K., Ishida, M., & Petre, R. 2002, *ApJ*, 572, 897
- Koyama, K., et al. 2007, *PASJ*, 59, 23
- Kushino, A., Ishisaki, Y., Morita, U., Yamasaki, N. Y., Ishida, M., Ohashi, T., & Ueda, Y. 2002, *PASJ*, 54, 327
- Li, H., & Chen, Y. 2010, *MNRAS*, 409, 35
- Masai, K. 1994, *ApJ*, 437, 770
- Matsumura, H., Uchida, H., Tanaka, T., Tsuru, T. G., Nobukawa, M., Nobukawa, K. K., & Itoh, M. 2017, *PASJ*, 69, 30
- Matsumura, H., Tanaka, T., Uchida, H., Okon, H., & Tsuru, T. G. 2017, *ApJ*, 851, 73
- Moriya, T. J. 2012, *ApJL*, 750, L13
- Morrison, R., & McCammon, D. 1983, *ApJ*, 270, 119
- Nakamura, R., et al. 2014, *PASJ*, 66, 62
- Nobukawa, K. K., et al. 2018, *ApJ*, in press (arXiv:1801.07881)
- Pannuti, T. G., et al. 2017, *ApJ*, 839, 59
- Rho, J., & Borkowski, K. J. 2002, *ApJ*, 575, 201
- Rho, J., & Petre, R. 1998, *ApJ*, 503, L167
- Sato, T., Koyama, K., Takahashi, T., Odaka, H., & Nakashima, S. 2014, *PASJ*, 66, 124
- Sato, T., Koyama, K., Lee, S.-H., & Takahashi, T. 2016, *PASJ*, 68, S8
- Sawada, M., & Koyama, K. 2012, *PASJ*, 64, 81
- Serlemitsos, P. J., Soong, et al. 2007, *PASJ*, 59, S9
- Shimizu, T., Masai, K., & Koyama, K. 2012, *PASJ*, 64, 24
- Slavin, J. D., Smith, R. K., Foster, K., Winter, H. D., Raymond, J. C., Slane, P. O., & Yanaguchi, H. 2017
- Seward, F. D. 1990, *ApJS*, 73, 781
- Tawa, N., et al. 2008, *PASJ*, 60, S11
- Torii, K., et al. 2011, *ApJ*, 738, 46
- Uchida, H., et al. 2012, *PASJ*, 64, 141
- Uchida, H., Koyama, K., & Yamaguchi, H. 2012, *PASJ*, 808, 77
- Uchiyama, H., Nobukawa, M., Tsuru, T. G., & Koyama, K. 2013, *PASJ*, 65, 19
- Velázquez, P. F., Dubner, G. M., Goss, W. M., & Green, A. J. 2002, *AJ*, 124, 2145
- Yamauchi, S., Nobukawa, K. K., Nobukawa, M., Uchiyama, H., & Koyama, K. 2016, *PASJ*, 68, 59
- Yamaguchi, H., Koyama, K., & Uchida, H. 2011, *PASJ*, 63, S837
- Yamaguchi, H., et al. 2014, *ApJL*, 785, L27
- Zhou, X., Miceli, M., Bocchino, F., Orlando, S., & Chen, Y. 2011, *MNRAS*, 415, 244
- Zhou, P., Safi-Harb, S., Chen, Y., Zhang, X., Jiang, B., & Ferrand, G. 2014, *ApJ*, 791, 87
- Washino, R., Uchida, H., Nobukawa, M., Tsuru, T. G., Tanaka, T., Nobukawa, K. K., & Koyama, K. 2016, *PASJ*, 68, S4
- White, R. L., & Long, K. S. 1991, *ApJ*, 373, 543
- Wooten, A. 1981, *ApJ*, 245, 105